The Journal of Experimental Biology 205, 2997–3008 (2002)
Printed in Great Britain © The Company of Biologists Limited
JEB4509

Fluid dynamics of flapping aquatic flight in the bird wrasse: three-dimensional unsteady computations with fin deformation

Ravi Ramamurti[1], William C. Sandberg[1], Rainald Löhner[2], Jeffrey A. Walker[3] and Mark W. Westneat[4]

[1]*Laboratory for Computational Physics and Fluid Dynamics, Naval Research Laboratory, Washington, DC 20375-5344, USA,* [2]*Computational Sciences and Informatics Department, George Mason University, Fairfax, VA 22030, USA,* [3]*Department of Biological Sciences, University of Southern Maine, Portland, ME 04103, USA* and [4]*Department of Zoology, Field Museum of Natural History, Chicago, IL 60605-2496, USA*

Accepted 9 July 2002

Summary

Many fishes that swim with the paired pectoral fins use fin-stroke parameters that produce thrust force from lift in a mechanism of underwater flight. These locomotor mechanisms are of interest to behavioral biologists, biomechanics researchers and engineers. In the present study, we performed the first three-dimensional unsteady computations of fish swimming with oscillating and deforming fins. The objective of these computations was to investigate the fluid dynamics of force production associated with the flapping aquatic flight of the bird wrasse *Gomphosus varius*. For this computational work, we used the geometry of the wrasse and its pectoral fin, and previously measured fin kinematics, as the starting points for computational investigation of three-dimensional (3-D) unsteady fluid dynamics. We performed a 3-D steady computation and a complete set of 3-D quasi-steady computations for a range of pectoral fin positions and surface velocities. An unstructured, grid-based, unsteady Navier–Stokes solver with automatic adaptive remeshing was then used to compute the unsteady flow about the wrasse through several complete cycles of pectoral fin oscillation. The shape deformation of the pectoral fin throughout the oscillation was taken from the experimental kinematics. The pressure distribution on the body of the bird wrasse and its pectoral fins was computed and integrated to give body and fin forces which were decomposed into lift and thrust. The velocity field variation on the surface of the wrasse body, on the pectoral fins and in the near-wake was computed throughout the swimming cycle. We compared our computational results for the steady, quasi-steady and unsteady cases with the experimental data on axial and vertical acceleration obtained from the pectoral fin kinematics experiments. These comparisons show that steady state computations are incapable of describing the fluid dynamics of flapping fins. Quasi-steady state computations, with correct incorporation of the experimental kinematics, are useful when determining trends in force production, but do not provide accurate estimates of the magnitudes of the forces produced. By contrast, unsteady computations about the deforming pectoral fins using experimentally measured fin kinematics were found to give excellent agreement, both in the time history of force production throughout the flapping strokes and in the magnitudes of the generated forces.

Key words: bird wrasse, *Gomphosus varius*, fin kinematics, flapping aquatic flight, unsteady flow, unstructured mesh, deforming fin.

Introduction

The pectoral fins power locomotion in many coral reef fishes over a wide range of speeds (Westneat, 1996; Walker and Westneat, 2000, 2002a,b). Swimming performance (determined in speed endurance tests for fishes) shows that pectoral propulsors in some species are capable of generating thrusts that can power speeds up to 10 body lengths s^{-1} (Walker and Westneat, 2002a,b). In addition, these species are highly maneuverable in complex three-dimensional reef habitats. Many reef fishes, including bird wrasse *Gomphosus varius*, fly underwater by flapping their pectoral fins with a motion that resembles the wing kinematics of several flying insects, including the hawkmoth *Manduca sexta* (Walker and Westneat, 1997). Walker and Westneat (2000) argued that this flapping motion is more mechanically efficient than the fore–aft rowing or paddling motion that is also common in fishes. Indeed, wrasses with flapping strokes can achieve and maintain higher pectoral-fin-powered swimming speeds than wrasses with rowing strokes (Walker and Westneat, 2002a,b).

In their earlier work on the mechanics of flapping fin propulsion in fishes, Walker and Westneat (1997) inferred fin

hydrodynamics by comparing detailed fin kinematics with measures of center-of-mass accelerations throughout the fin stroke cycle. They used the center of mass accelerations in place of direct measurements of the instantaneous force balance, because the latter cannot be measured on a freely swimming animal. The vector of instantaneous center-of-mass acceleration differs from the vector of net forces at the center of mass by a constant, hence the pattern of thrust and lift occurring throughout the stroke will be the same, regardless of whether this is directly measured with a force transducer or estimated by center-of-mass kinematics. More recently, the dynamics of pectoral fin propulsion in the bluegill *Lepomis macrochiris* and surfperch *Embiotoca jacksoni* was investigated using digital particle image velocimetry (DPIV) of the wake (Drucker and Lauder, 1999, 2000). These wake studies have proved useful in exploring the fluid dynamic events occurring at the fin.

In this study, we seek to complement these experimental studies of fin kinematics, center-of-mass dynamics and wake visualization by computing the unsteady flow about *G. varius* with pectoral fin oscillation and deformation prescribed from the experimental kinematics. We continue our earlier computational focus on oscillating control surface flows for non-undulating bodies, using *G. varius*. The primary objectives in this work are to (i) investigate the fluid dynamics underlying the generation of forces during pectoral fin oscillation, (ii) compare the hydrodynamic utility of steady, quasi-steady and unsteady hydrodynamic models of fin propulsion, and (iii) to compare the fluid dynamics of a flapping appendage during forward motion with a flapping appendage during hovering.

For this last objective, we note that the results are relevant not only to fish propulsion but also to the locomotion of any animal moving with oscillating appendages in a similar fluid-dynamic environment. For example, *G. varius* at the large end of the size range investigated by Walker and Westneat (1997, 2002a,b) has approximately the same mass and flaps with approximately the same reduced frequency and Reynolds number as *M. sexta* (Willmott et al., 1997). Both *G. varius* and *M. sexta* wings are stiff along their span. *G. varius* flaps its wings along a steeper stroke plane than *M. sexta*, although at the high end of the latter's flight speed these values converge. Finally, while the wing of *M. sexta* has a greater aspect ratio than that of *G. varius*, the radial moments of area are the same (see corrected values for *G. varius* in Walker and Westneat, 2002b).

Materials and methods

The incompressible flow solver

The governing equations employed are the incompressible Navier–Stokes equations in Arbitrary Lagrangian Eulerian (ALE) formulation, written as:

$$\frac{\partial \mathbf{v}}{\partial t} + \mathbf{v}_a \cdot \nabla \mathbf{v} + \nabla p = \nabla \cdot \sigma \,, \quad (1)$$

$$\nabla \cdot \mathbf{v} = 0 \,, \quad (2)$$

where p denotes the pressure, $\mathbf{v}_a = \mathbf{v} - \mathbf{w}$ is the advective velocity vector (where $\mathbf{v}$ is flow velocity and $\mathbf{w}$ is mesh velocity), and both the pressure p and the stress tensor σ have been normalized by the (constant) density ρ, are discretized in time using an implicit time-stepping procedure. Thus the equations are Eulerian for zero mesh velocity and Lagrangian if the mesh velocity is the same as the flow velocity. The present time-accurate flow solver is discretized in space using a Galerkin procedure with linear tetrahedral elements. The details of the flow solver are discussed extensively elsewhere (Ramamurti and Löhner, 1992; Ramamurti et al., 1994, 1995, 1999) in connection with successfully validated solutions for numerous 2-D and 3-D, laminar and turbulent, steady and unsteady flow problems.

Unstructured mesh generation and adaptive re-meshing

In order to carry out computations of the flow about oscillating and deforming geometries, which may be quite complex, several pieces of grid technology are needed. First, one must be able to rapidly generate a surface triangulation. If many complex surfaces are intersecting and they are discrete components, as is the case for multiple fins on a fish body, it is essential to be able to construct the total surface mesh, including the intersection loci, automatically. One then needs to describe the mesh motion on the moving surface, couple the moving surface mesh to the volume grid in a smoothly varying manner, and describe the dynamic remeshing of the volume grid in proximity to the moving surface as the surface moves and deforms. In deformations, the surface motion may be severe, leading to distorted elements in the absence of remeshing, which in turn lead to poor numerical results. If the bodies in the flow field undergo arbitrary movement, a fixed mesh structure will lead to badly distorted elements. This means that at least a partial regeneration of the computational domain is required. On the other hand, if the bodies move through the flow field, the positions of relevant flow features will change. Therefore, in most of the computational domain a new mesh distribution will be required.

One approach to solving these problems is to add several layers around the moving bodies that move rigidly with the body. As the elements (or edges) move, their geometric parameters (shape–function derivatives, jacobians, etc.) need to be recomputed at every timestep. If the whole mesh is assumed to be in motion, then these geometric parameters need to be recomputed globally. In order to reduce the number of global remeshings and hence save computational time when using this approach, only a small number of elements surrounding the bodies are actually moved. The remainder of the field is then treated in the usual Eulerian frame of reference, avoiding the need to recompute geometric parameters. We refer the reader to earlier paper (Löhner, 1998) that discuss the mathematics and numerics of the unstructured grid generation and adaptive remeshing codes used in this work.

Fish

The *G. varius* Lacepède 1801 individual was acquired from

a tropical fish wholesaler and maintained in a 228 l aquarium within a 2300 l recirculating marine system until it was euthanised with an overdose of MS-222 (Finquel brand, Aldrich Chemical Co.) and frozen at −20°C.

Three-dimensional wrasse body and pectoral fin description

To obtain the 3-D surface coordinates of a bird wrasse, an individual of standard length L=21 cm was frozen and sliced into nine transverse sections. Section outlines were digitized using a modification of the public domain NIH Image program (developed at the US National Institutes of Health and available on the Internet at http://rsb.info.nih.gov/nih-image/) for the Apple Macintosh (the modification is available upon request from J. A. Walker). The outline coordinates were used to generate a smooth surface using standard cubic spline methods. While the digitized individual is representative of the geometry of the subjects from the experiment (Walker and Westneat, 1997), it was not one of the experimental subjects. The exact geometry and the corresponding surface mesh of the bird wrasse for which the computations were done are shown in Fig. 1.

Pectoral fin kinematics data

Pectoral fin surface coordinates were estimated from the experimental data. In the original experiment of Walker and Westneat (1997), five aluminum markers were attached to one of the pectoral fins: two on the leading edge, two on the trailing edge and one on the fin tip. Fin motion was filmed using S-VHS videotape at 60 Hz. The five fin markers and the dorsal base of the pectoral fin were digitized from both lateral and dorsal views. The 3-D coordinates of the markers throughout the cycles were obtained from the marker positions in the two views. For the present analysis, the motion of the three distal-edge markers was smoothed with a quintic spline function (Walker, 1998). In order to remove the kink in the distal (tip) edge of the fin that necessarily resulted from having only three digitized points, a smooth curve was fitted to the distal edge by increasing the number of points to 14 (the number of fin rays in the fin), using linear interpolation and smoothing the distal edge with a quintic spline function (Walker, 1998). 3-D surface coordinates were obtained by linear interpolation between the digitized pectoral fin base of the representative individual, scaled to the size of an experimental individual, and the distal edge of an experimental individual.

Walker and Westneat (1997) observed that the fins flapped synchronously during rectilinear motion at all test speeds. They also noted that *G. varius* flapped its pectoral fins up and down with a small anterior movement during abduction and a small posterior movement during adduction. Flapping frequency was seen to increase linearly with speed. The mean flapping frequency was 2.9 Hz at 22 cm s^{-1} and 4.2 Hz at 50 cm s^{-1}. In the computations carried out here, we used a pectoral fin-oscillation frequency of 3.3 Hz, corresponding to a swimming speed of approximately 45 cm s^{-1} (2 L s^{-1}). The digitized

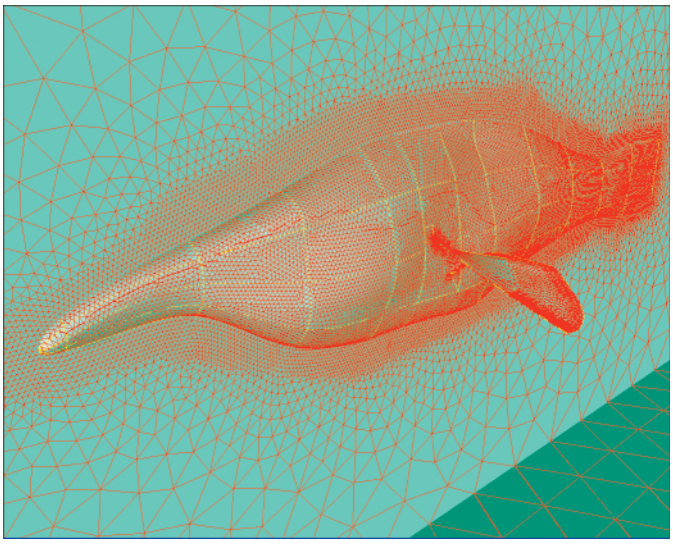

Fig. 1. Computational surface mesh for body and pectoral fin.

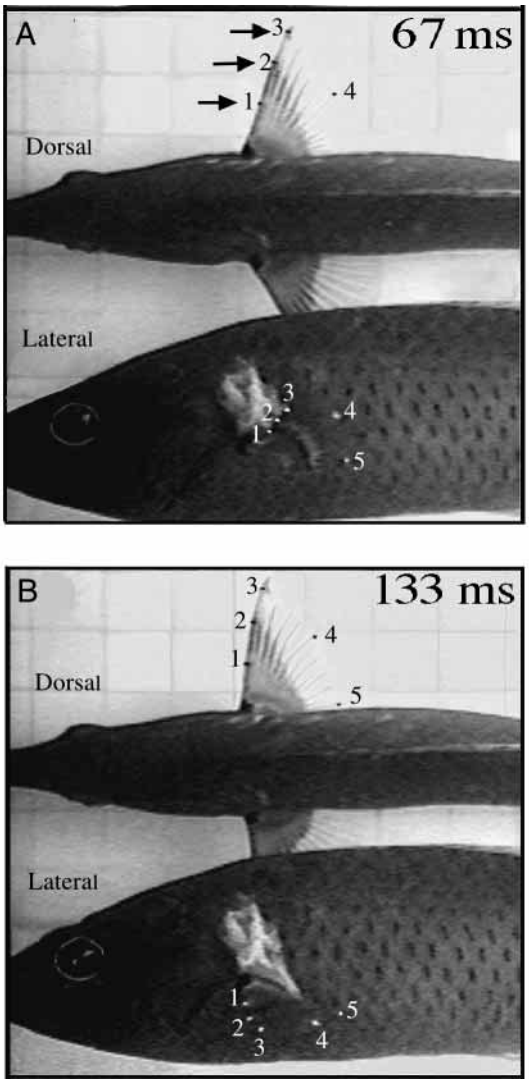

Fig. 2. Pectoral fin and markers during (A) mid-phase and (B) late phase of downstroke.

positions of the five markers throughout the oscillation cycle served to specify the kinematics of the pectoral fin for the present computations. Photographs showing dorsal and lateral views of fin geometry at two extended positions during the cycle are shown in Fig. 2.

Results and Discussion

Computational results

A set of steady computations were carried out at selected times during the fin-oscillation cycle using the incompressible flow-solver described above. These computations were necessary to establish a baseline and to assess the acceptability of the computational mesh. The results for a representative case of maximum fin extension are given. Surface velocity vectors and particle traces for this steady flow situation are shown in Fig. 3. The computational mesh consisted of 152,386 points and 832,830 tetrahedral elements. Previous grid refinement studies in the computation of the flow over a tuna with caudal fin oscillation (Ramamurti et al., 1996, 1999) showed that this mesh is sufficient for resolving the inviscid flow past this configuration. Since the steady flow cases are not representative of actual pectoral fin locomotion flows, they will not be discussed in detail. A complete discussion of the steady flow computational results and a comparison with the quasi-steady flow computational results has been presented elsewhere (Sandberg et al., 2000). For completeness, and to demonstrate the inadequacy of steady and quasi-steady flow computations for this problem, the computed steady forces are compared with those for the quasi-steady and unsteady computations below.

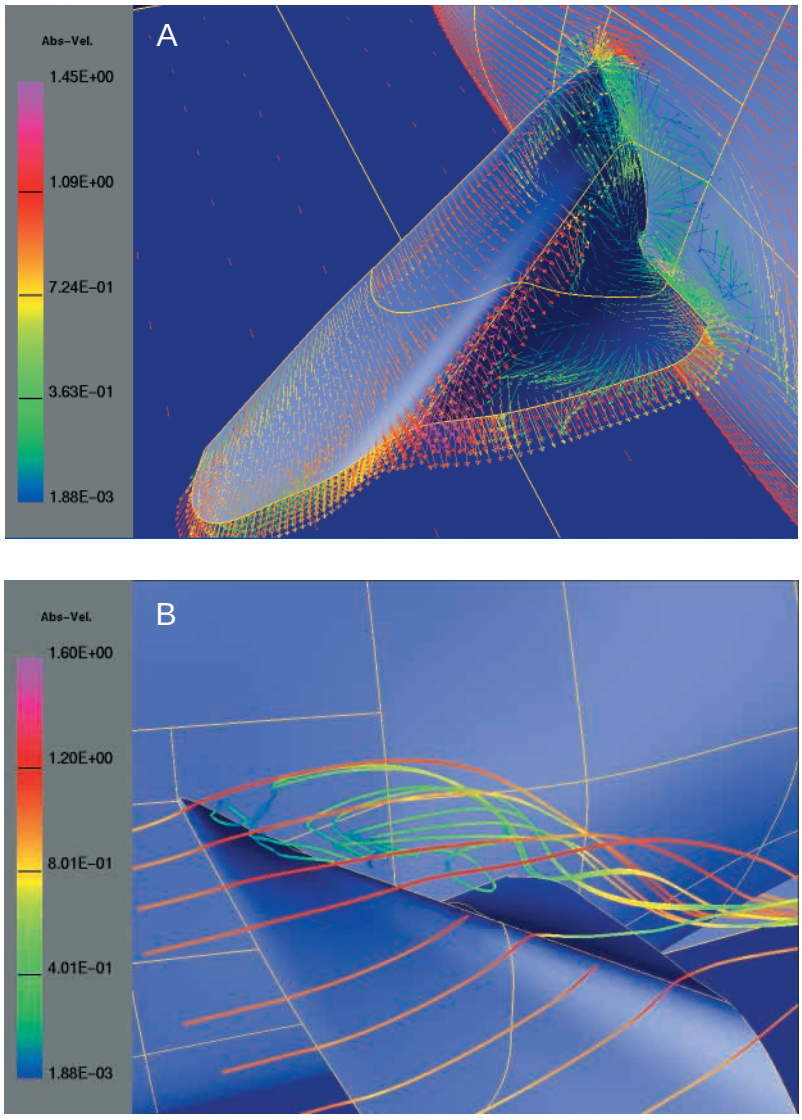

Fig. 3. Steady-state flow past the pectoral fin. The position of the fin corresponds to t=0.15 s. (A) Velocity vectors on the surface of the pectoral fin. The vectors are colored according to the magnitude of velocity and are of constant length. The velocity vector is non-dimensionalized with respect to the swimming velocity. (B) Particle traces past a fully extended pectoral fin. Particles are released along a rake parallel to and just upstream of the leading edge of the fin. These particle traces are colored according to the magnitude of velocity.

Quasi-steady computations

A set of quasi-steady computations were carried out, as an intermediate step, to determine the differences between steady state computations for the fin at fixed positions and angles of attack and computations also incorporating fin kinematics data. The positions of the pectoral fin at selected times during both abduction (downstroke) and adduction (upstroke), shown in Fig. 4, were chosen for the quasi-steady computations. To simulate the quasi-steady state solution at any instant of time, the velocity of the fin was obtained from the experimental kinematics data at that instant. This velocity was then used as the mesh velocity at the fin surface, without actually moving the fin surface. The computed flow solution is thus the steady state flow with the high velocity motion of the fin superimposed on it. (Note that this is not the usual approach taken for what is termed ‘quasi-steady’ in the literature. Usually the flow is merely computed about the geometry at successive angles of inflow, using the same steady inflow velocity for each angle of attack, thus neglecting the induced velocity due to the fin kinematics.) Forces on the pectoral fin and the fish body were computed, for the quasi-steady simulation, for each orientation of the fin, by integrating the surface pressures.

Comparison of the steady flow forces and those from the quasi-steady flow computation (Fig. 5) shows a considerable difference. Fig. 5A shows the coefficients of the thrust and lift obtained from the steady state computation at several time instants throughout the stroke cycle. The steady state flow was computed with the fin fixed at the corresponding position with the mesh velocity, $\mathbf{w}_{fin}$=0. The computations resulted in a net drag (as

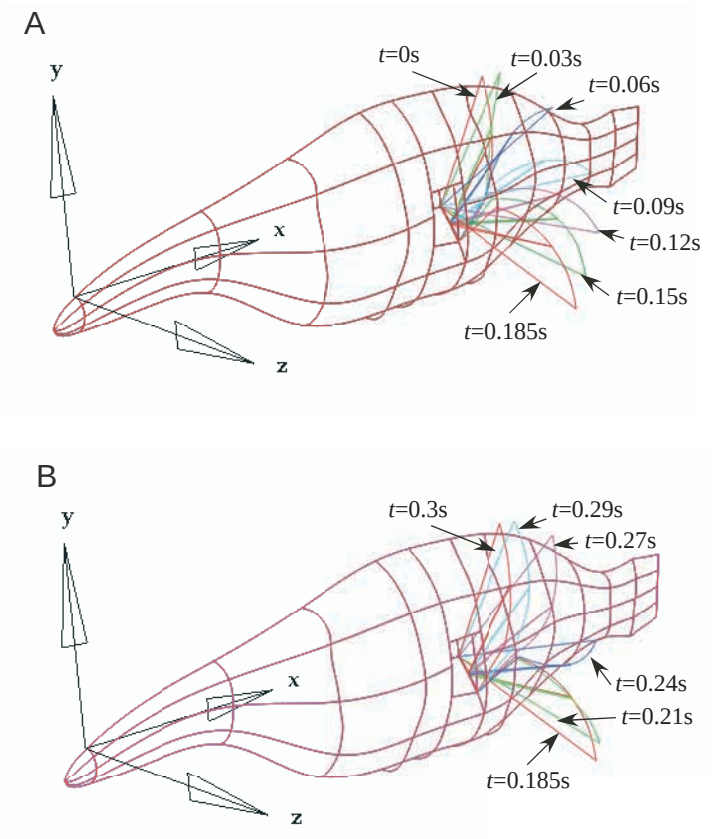

Fig. 4. Pectoral fin location at various times *t* throughout the stroke cycle. (A) Downstroke (abduction). (B) Upstroke (adduction).

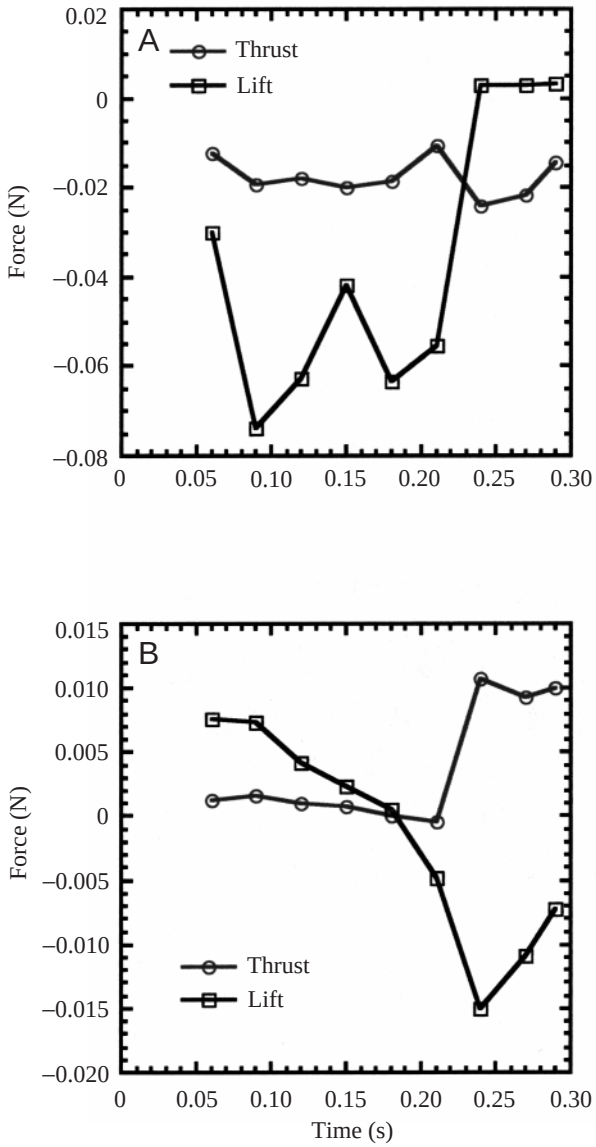

Fig. 5. Variation of thrust and lift forces. (A) Steady state computations. (B) Quasi-steady state computations.

opposed to thrust from the quasi-steady computations) for all the orientations considered throughout the stroke cycle. The computed lift is negative for fin orientations up to t=0.2 s and is positive thereafter.

We next investigated whether either of these computations was in agreement with the experimental data. The trend of the quasi-steady computed forces, Fig. 5B, reproduces the trend of the experiments. For example, the center-of-mass acceleration data (fig. 5 of Walker and Westneat, 1997) indicates that there is a large upward vertical force during the downstroke, a large negative vertical force during the upstroke, and a large positive thrust during the upstroke. In addition, it was found in the experiments that the maximum upward vertical force during abduction occurred between 30–40% of the abduction phase, the maximum downward vertical force during adduction occurred at approximately 40% of the adduction and the maximum thrust also occurred at 40% of the adduction phase. All of these maxima are observed in Fig. 5B to occur at about the same times in the computational cycle, as was observed in the swimming experiments. This agreement between the experimental and computed times and signs of force maxima and minima is to be expected if accurate experimental kinematics are incorporated correctly into the quasi-steady computation. Assuming the mass of the fish to be 100 g, the peak vertical acceleration from the computed forces is 7.5 cm s^{-2} during the abduction phase and 15 cm s^{-2} during the adduction phase. The experimental peak values are in the range 70–100 cm s^{-2}. From the quasi-steady computed forces, the peak fore–aft acceleration is 10.5 cm s^{-2}, compared to the experimental range of 40–80 cm s^{-2}. Hence, the magnitudes of the quasi-steady computed forces are not correct. Thus, true quasi-steady computations are useful but, because 3-D inertial forces are neglected, not sufficient. Unsteady computations must be performed.

Unsteady computations

Unsteady computations were also carried out using the prescribed fin kinematics. A new mesh-movement capability, to accommodate the deforming fin surface, was developed and added to the mesh-movement algorithm used in earlier flapping-fin computations (Ramamurti and Sandberg, 2001, 2002; Sandberg and Ramamurti, 2001). The motion of the fin

surface was first prescribed at a finite set of control points. The Cartesian coordinates on the fin surface were then transformed to a parametric space. The coordinates of the surface points were maintained constant in the parametric space throughout the computation, while the Cartesian coordinates were computed according to the prescribed motion of the control points.

Unsteady simulations were carried out with the bird wrasse swimming at 45 cm s^{-1}. The stroke amplitude is approximately 2.14 rad and the frequency of fin oscillation is 3.3 Hz, resulting in a mean tip speed of approximately 50 cm s^{-1}. The computation was carried out for more than four cycles of fin oscillation using a computational mesh consisting of approximately 150×10^3 points and 840×10^3 tetrahedral elements.

At the beginning of the downstroke, the fin is quite close to the body and it is difficult to clearly visualize the fin flow field, hence these time steps have not been included. The simulation of the pectoral fin motion was actually begun slightly after the start of the downstroke, at t=0.05 s, rather than at t=0 s, to avoid the difficulties associated with contact of the fin and the body surfaces. This is considered to have almost no influence on the magnitude of the forces, since the experimentally observed fore–aft accelerations are in the range 0–20 cm s^{-2}. A Navier–Stokes computation to estimate the pressure and viscous drag on the body yielded a total drag of 1.6 kg. The aft acceleration for a 100 g fish is 16 cm s^{-2}, suggesting that the force production due to the fin at this instant is negligible.

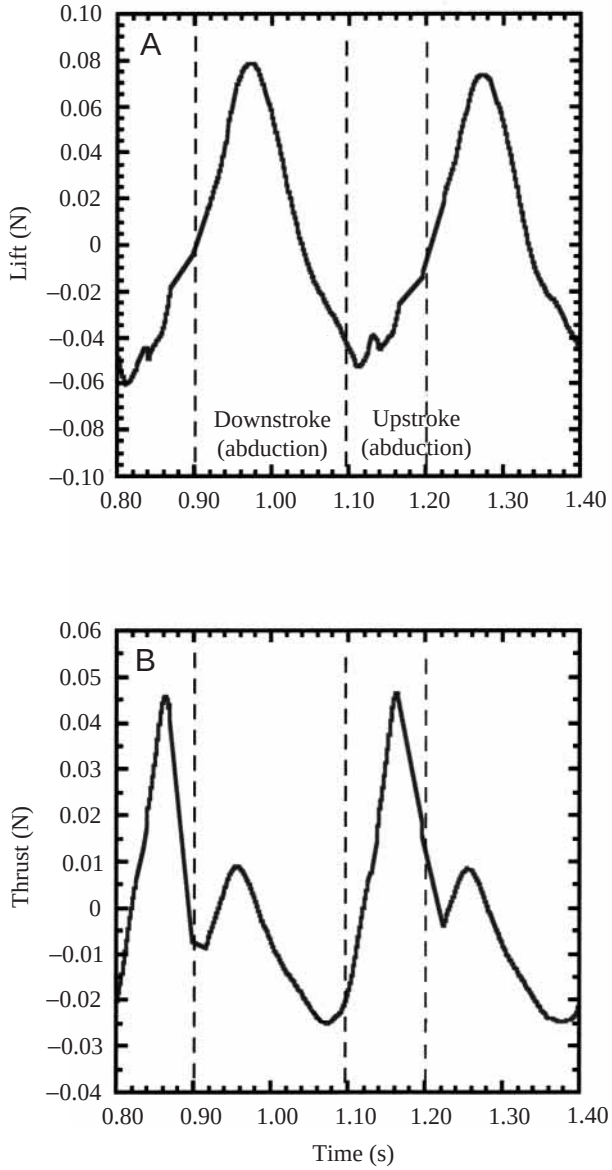

Fig. 6. Time variation of unsteady (A) lift and (B) thrust forces.

The time-varying 3-D lift and thrust (Fig. 6) were computed by integrating the surface pressure over the wrasse body and fin at each time step throughout the simulation. It was noticed that the experimentally specified kinematics at the point where the fin is closest to the fish body were not continuous. This is because the downstroke is steeper than the upstroke, and occurs at the end of the upstroke. This discontinuity, however, does not alter the essential aspects of force production and hence constitutes only a minor perturbation to the results. The computed lift and thrust from the unsteady simulations (Fig. 6) are much larger than those from the quasi-steady simulation (Fig. 5). The peak thrust from the unsteady computations is 0.045 N, compared to 0.01 N in the quasi-steady computations. The unsteady lift varies between –0.06 N and 0.08 N, while those for the quasi-steady computation range between –0.015 N and 0.0075 N.

The velocity vectors on the entire wrasse and its pectoral fin are shown in Fig. 7A. The body flow at this instant is typical of that observed throughout the stroke cycle. The flow over most of the wrasse body is observed to be uniform throughout the stroke cycle, with a recirculating flow region at the junction of the pectoral fin and the body. The highest velocities are observed on the pectoral fin, above the root of the fin, and on the dorsal side just anterior to the caudal fin.

A closer view of the pectoral fin flow is given in Fig. 7B–F at critical times during the cycle. Fig. 7B shows the flow velocity vectors at t=0.963 s (32% of the downstroke), when the thrust reaches a maximum. In addition to the junction vortex, we see the wake of the previous upstroke on the body downstream of the fin. Fig. 7C shows the velocity vectors on the pectoral fin at t=1.065 s, which occurs at approximately 84% through the downstroke. This is the time of minimum total force production on the downstroke. A clockwise flow is seen at the root above the leading edge and a large recirculation region is present between the fin and the body. In addition to this separated flow region, a small recirculating region can be seen at the junction of the trailing edge of the fin and the body. Fig. 7D shows the velocity vectors occurring at t=1.1021 s, which corresponds approximately to the beginning (8%) of the upstroke, and the magnitude of the velocity on the upper surface has increased. We observe that, despite the counterclockwise flow on the surface behind the leading edge near the fin root, the clockwise flow on the wrasse body above the root remains. Fig. 7D shows the velocity vectors at t=1.140 s, corresponding to 43% of the

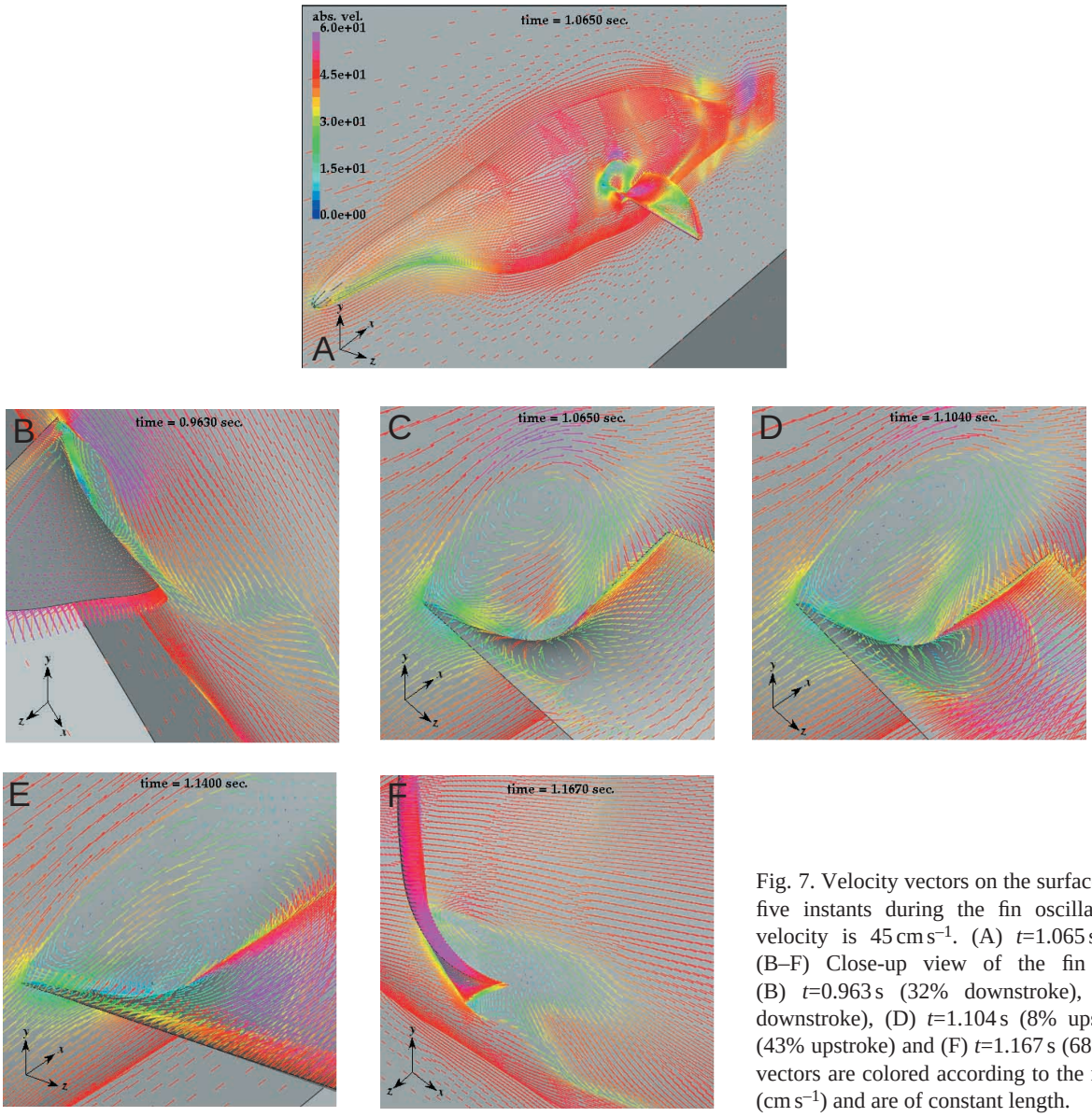

Fig. 7. Velocity vectors on the surface of the bird wrasse at five instants during the fin oscillation. The swimming velocity is 45 cm s^{-1}. (A) t=1.065 s (84% downstroke). (B–F) Close-up view of the fin and body junction. (B) t=0.963 s (32% downstroke), (C) t=1.065 s (84% downstroke), (D) t=1.104 s (8% upstroke), (E) t=1.140 s (43% upstroke) and (F) t=1.167 s (68% upstroke). Velocity vectors are colored according to the magnitude of velocity (cm s^{-1}) and are of constant length.

upstroke; the recirculation region from the leading edge of the fin is elongated along the body and the region on the surface of the fin is reduced. Also, the vortex near the body-trailing edge junction has formed again. At the instant when the thrust is maximum during the upstroke, t=1.167 s (68% of the upstroke), the interaction of the wake from the upstroke and the body can be seen in the low velocity regions on the body.

In order to provide additional information on the flow about the fin during times of peak force production, we also examined the surface pressure contours. Fig. 8 shows the surface pressure contours, in N m^{-2}, on the pectoral fin at three instants when the peak in the thrust occurs. At t=0.963 s (32% of the downstroke) (Fig. 8A,B), maximum and minimum pressures occur below and above the leading edge of the fin, respectively, producing maximum thrust (in the $-x$ direction) and lift (in the $+y$ direction). At t=1.065 s (84% of the downstroke) (Fig. 8C,D), maximum and minimum pressures occur above and below the leading edge, respectively, in the outer half-span of the fin, producing minimum thrust. At t=1.167 s (68% of the upstroke) (Fig. 8E,F), a high pressure region extends for more than half of the fin on the dorsal side, while the pressure on the ventral side is almost uniform with a region of minimum pressure near the outer leading edge, producing a maximum thrust.

The wake of the pectoral fin in the z=1.5 cm plane is shown at critical instants during the oscillation in Fig. 9. The swimming velocity of the fish (45 cm s^{-1}) is subtracted from the x component of the velocity to reveal the vortical structures. These are qualitatively similar to the patterns observed by Drucker and Lauder (1999, 2000) in the wake of a surfperch. A quantitative analysis of the wake vortex structure can be performed after a Navier–Stokes computation of the flow and will be presented in a later work. At the beginning of the

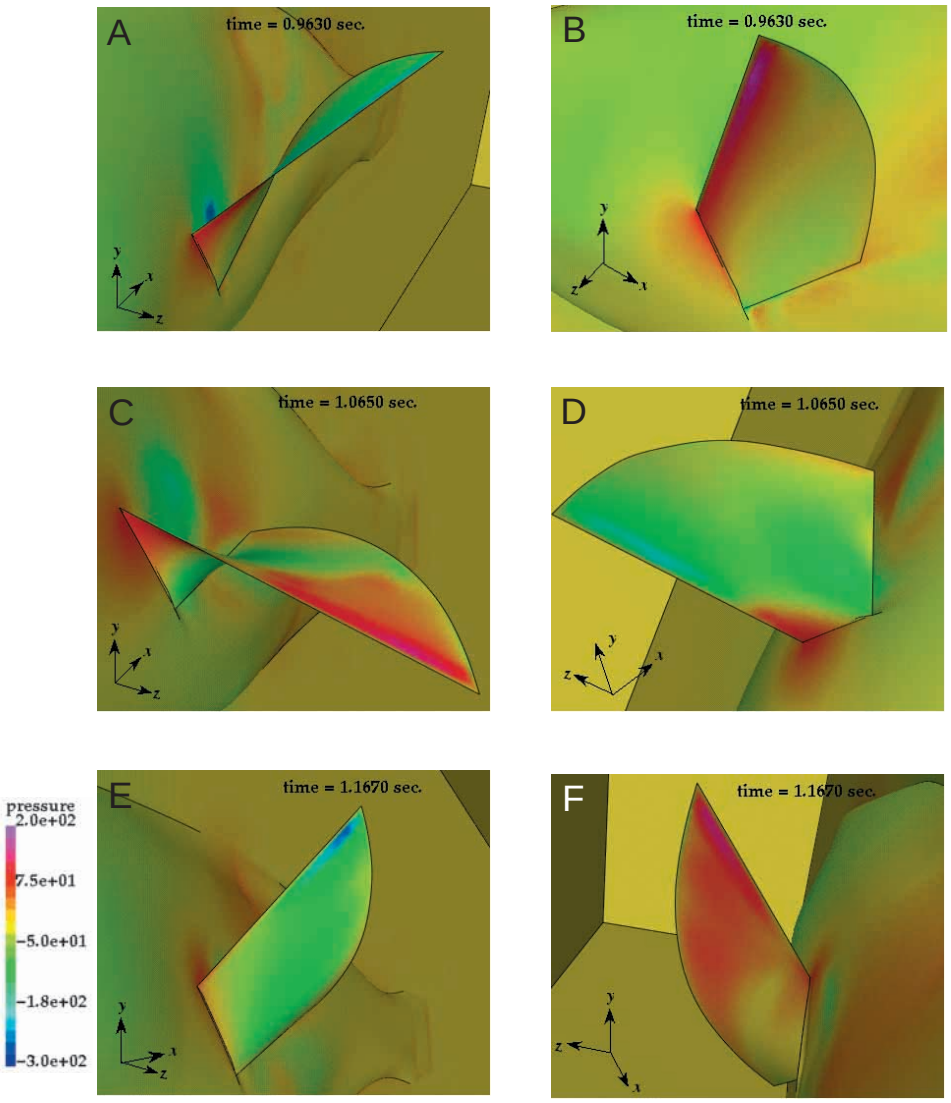

Fig. 8. Surface pressure contours ($N\,m^{-2}$) on the pectoral fin at three instants when the peak in the thrust occurs. (A,C,E) Front, (B,F) back, (D) ventral view. (A,B) t=0.963 s (32% downstroke); maximum and minimum pressure occur below and above the leading edge of the fin, respectively, producing maximum thrust (–x direction) and lift (+y direction). (C,D) t=1.065 s (84% downstroke); maximum and minimum pressure occur above and below the leading edge, respectively, in the outer half span of the fin, producing minimum thrust. (E,F) t=1.167 s (68% upstroke); high-pressure region extends for more than half the dorsal side of the fin while the pressure on the ventral side is almost uniform, with a region of minimum pressure near the outer leading edge, producing a maximum thrust.

downstroke, two counter-rotating vortices are observed at t=0.906 s, Fig. 9B. These vortices are shed from the distal edge on the previous upstroke. A large leading edge vortex spanning the entire chord is observed on the suction side in Fig. 9C at t=1.065 s, (84% of the downstroke). The thrust reaches a minimum at this instant. Fig. 9D shows a vortex being shed from the trailing edge at t=1.14 s (43% of the upstroke). During the middle of the stroke, the distal edge acts like the trailing edge, hence, we term this a ‘trailing edge’ vortex. The shedding of this trailing edge vortex into the wake leads to a momentary increase in lift (Fig. 6A). At t=1.167 s (68% of the upstroke), the trailing edge vortex is convected downstream. Also, the chord at this instant is aligned so that the high pressure produced by the leading edge vortex on the dorsal side of the fin produces a maximum thrust. Prior to stroke reversal, at t=1.197 s, two vortices are shed from the distal edge.

As an additional diagnostic for the flow at the leading edge we plotted the instantaneous particle traces in the middle of the downstroke (Fig. 10B) and just after the stroke reversal (Fig. 10C). Particles are released from a rake of rectangular grid of points 0.75 cm away from the leading edge of the fin and parallel to it, as shown in Fig. 10A. We observed a vortex on the ventral side of the fin just after stroke reversal (Fig. 10C). There was no indication of a strong spanwise flow, which would exist if a leading-edge spiral vortex was present. Our flapping wing computations for *Drosophila melanogaster* (Ramamurti and Sandberg, 2002) also showed no evidence of a spiral leading-edge spanwise vortex. This suggests that the dynamics of force generation in the pectoral fin of the swimming wrasse is different from the fluid dynamics of force production in the hovering hawkmoth. A leading-edge spiral vortex with spanwise flow was seen by Ellington et al. (1996) in their wind-tunnel experiments on tethered hawkmoths. The spanwise flow in the vortex core has been proposed as the mechanism for stabilization of the leading edge vortex. In our case, as can be seen from the surface velocity vectors and particle traces, we are clearly more dominated by the axial flow than is the case for the hovering hawkmoth.

We also computed the fore–aft and dorso–ventral accelerations of the fish, assuming a mass of 100 g, from the

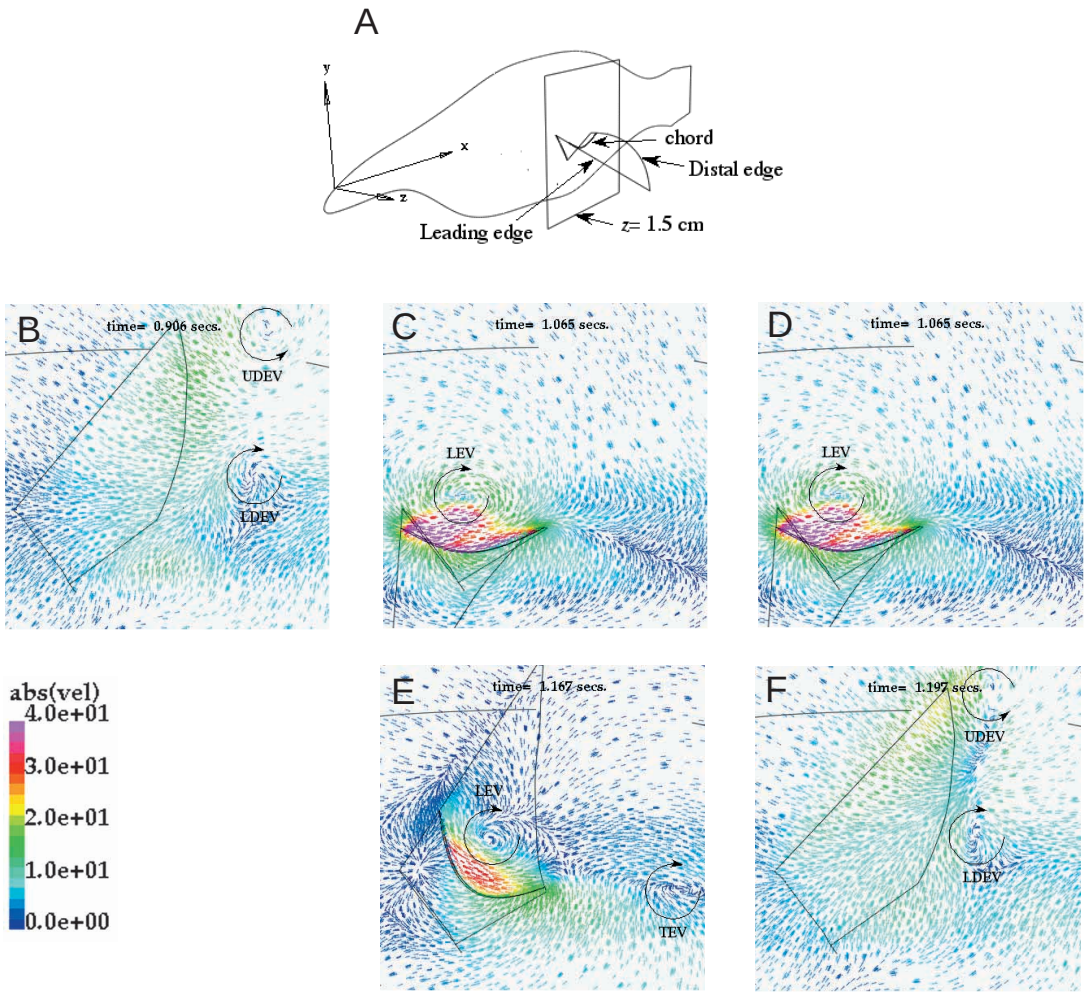

Fig. 9. (A) The orientation of the pectoral fin showing the leading and distal edges and the z=1.5 cm plane, for which the in-plane velocity components (cm s^{-1}) are shown. The swimming velocity of the fish (45 cm s^{-1}) is subtracted from the x component of the velocity to reveal the vortical structures. (B) Two counter-rotating vortices are observed at t=0.906 s, just after stroke reversal. These are shed from the distal edge on the previous upstroke. (C) A large vortex spans the entire chord at t=1.065 s, when the thrust is minimum. (D) A vortex is shed from the trailing edge midway during the upstroke, t=1.14 s, leading to a momentary increase in lift force. (E) At t=1.167 s, 68% upstroke, the TEV is convected downstream. (F) At t=1.197 s, prior to stroke reversal, two vortices are shed from the distal edge. UDEV, upper distal edge vortex; LDEV, lower distal edge vortex; LEV, leading edge vortex; TEV, trailing edge vortex.

thrust and lift (Fig. 11), and compared them with the experimentally derived fore–aft acceleration results for the 47 cm s^{-1} data from fig. 5A of Walker and Westneat (1997). We found the computational results to be in good agreement with the data from the swimming experiments. The principal observations from the comparison between the computed results and those from the experiments are presented below.

Axial forces and accelerations

An aft acceleration is observed experimentally throughout the downstroke for the 47 cm s^{-1} data set. The maximum value of the aft acceleration, which ranges between 20–45 cm s^{-2}, occurs at approximately one quarter of the downstroke, and again just after the three-quarters region of the downstroke. The aft acceleration decreases to approximately zero near mid-stroke, and again at the end of the downstroke. The acceleration data for the other swimming speeds all show a small acceleration, which is aft-directed at first, then changes sign but has a small magnitude, and then becomes aft-directed for the remainder of the downstroke (see fig. 5A of Walker and Westneat, 1997).

The computed axial acceleration starts near zero (Fig. 11A) as the downstroke begins and increases to a maximum at about 30% of the downstroke. It then decreases, going through zero acceleration to an aft-directed acceleration for the remainder of the downstroke. The maximum aft-directed acceleration occurs at about 90% through the downstroke, in excellent agreement with the data. The small forward-directed acceleration peak that we observe from the computations is not present in the data. Adding the viscous body and fin drag to our computed drag values reduces all the positive accelerations

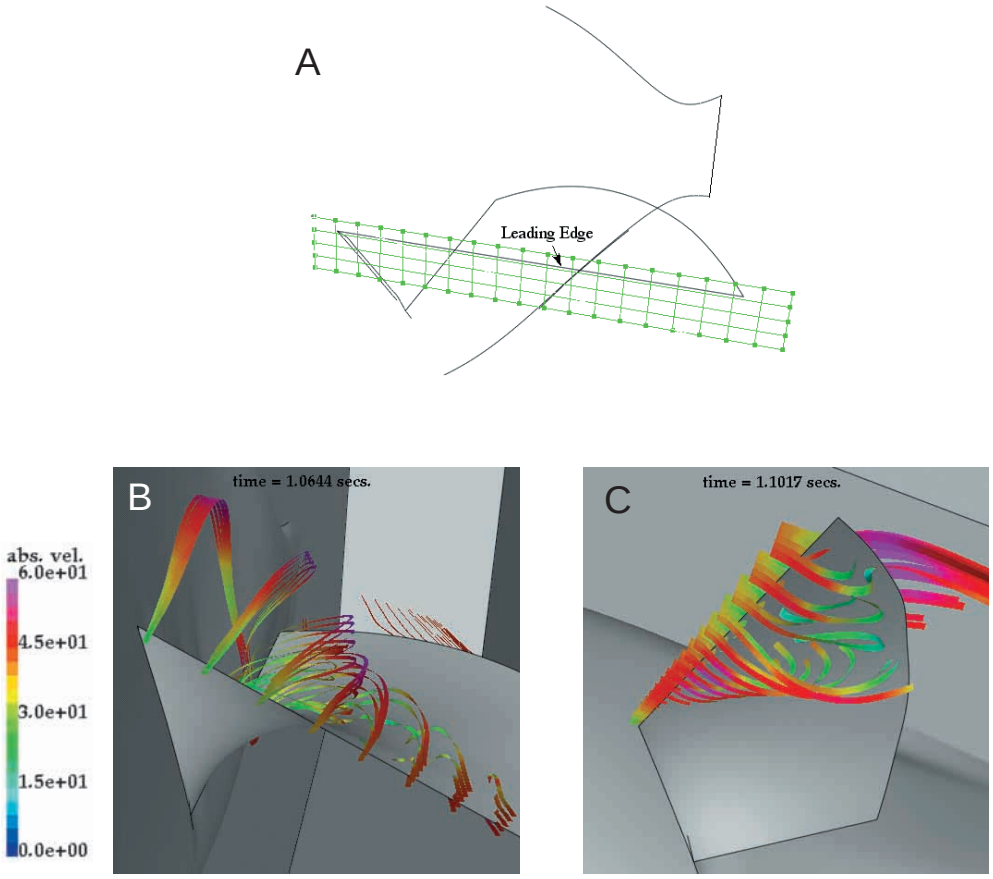

Fig. 10. Instantaneous particle traces are released from (A) a rake of rectangular grid of points in a plane 0.75 cm away from the leading edge of the pectoral fin and parallel to it. Using the instantaneous velocity field, the positions of theses particles were obtained by integrating the velocity at these points until the length of these traces exceeded a specified length, or the particles ended on a solid boundary, or exited the computational domain. These particle traces are colored according to the magnitude of velocity (in cm s^{-1}) at that location. (B) Middle of the downstroke, t=1.064 s. (C) Beginning of the upstroke, t=1.1017 s.

and increases the aft-directed accelerations. We made a conservative estimate of the body and fin viscous drag throughout the swimming cycle by carrying out a Navier–Stokes drag computation for the fully extended fin case. The Reynolds number for this simulation is set to be approximately 16,000, based on the pectoral fin length and a fish swimming speed of 45 cm s^{-1}. The fully extended pectoral fin configuration corresponds to an instant during the middle of the downstroke. This computation yields a body viscous drag of 1.05×10^3 g and a fin viscous drag of 2.20×10^3 g, which corresponds to an aft-directed axial acceleration for the 100 g fish of 32.5 cm s^{-2}, which exceeds the magnitude of the positive peak. This value cannot be subtracted from any points on the acceleration curve since it is a steady result and thus, strictly speaking, cannot be used to alter the computed unsteady results. It does, however, serve to indicate that at some point during both the upstroke and the downstroke, a viscous drag force of approximately this magnitude would be experienced by the wrasse. It therefore also indicates that if an unsteady Navier–Stokes computation were performed, one would have a substantially lower positive region, or possibly no positive region, during the downstroke.

The computed results for fore–aft acceleration during the upstroke agree well with the experimental results. The experiments show an increase in forward acceleration, to a maximum occurring between 40–50% of the upstroke, then decreasing steadily to zero at approximately 90% of the upstroke. The maximum accelerations from the experiments were in the range 30–90 cm s^{-2}. A forward acceleration maximum of approximately 45 cm s^{-2} was obtained at approximately 68% of the upstroke (Fig. 11A), with the acceleration decreasing steadily toward zero at the beginning of the downstroke.

Dorso–ventral acceleration

We also compare our computed results for dorso–ventral acceleration (Fig. 11B) with that from fig. 5B of Walker and Westneat (1997). The distributions of accelerations for fishes swimming at 47 cm s^{-1} rise from a negative value at the start of abduction (downstroke) to a maximum dorsal acceleration at about 44% abduction, decreasing to zero at about 80%, and becoming negative through the remainder of the downstroke. The range of the maximum dorsal acceleration is 70–100 cm s^{-2}, and that of the ventral accelerations at the start of abduction is 10–30 cm s^{-2}. Our computed results show a ventral (downward) acceleration at the start of the downstroke, rising to a maximum dorsal acceleration at about 40% abduction, and then decreasing to zero at about 70% abduction and steadily becoming negative. The magnitude of the computed dorsal acceleration is approximately 80 cm s^{-2} and the ventral acceleration at the start of abduction is approximately 40 cm s^{-2}. Again there is excellent agreement with the experimental results.

It should also be noted here that the mass of the fish we used

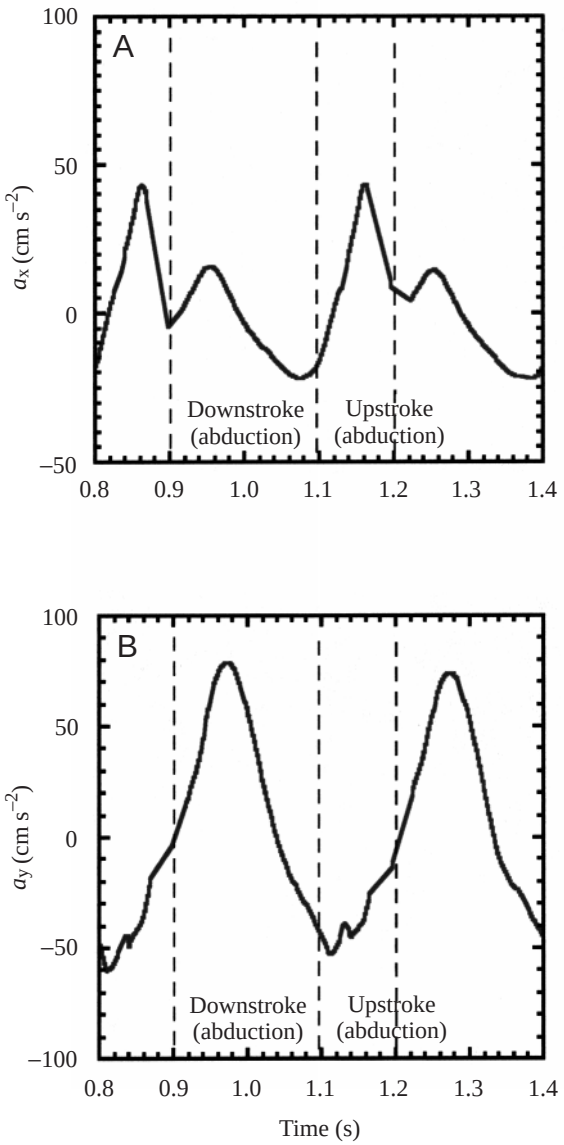

Fig. 11. Time variation of (A) fore–aft acceleration a_x and (B) dorso–ventral acceleration a_y.

in our computations, 100 g, was not a mass of any of the fish population making up the 47 cm s^{-1} data. The masses of the fish making up the 47 cm s^{-1} data were 24–50 g, hence we did not actually compare our computations against the data for any specific fish in the original experiments, but rather we claim that our computed fish dynamics are representative of the dynamics observed experimentally for the bird wrasse as a species. Since the unsteady computations are in good agreement with the results from the swimming experiments, we conclude that inertial effects, ignored in the quasi-steady computations, are quite significant in the thrust- and lift-generation processes.

Summary and conclusions

We computed the unsteady dynamics about a bird wrasse with flapping and deforming pectoral fins using a new moving-mesh capability for unstructured adaptive meshes. The unsteady computations were compared with steady state computations, quasi-steady state computations and experimental results. We found that the steady state computations are incapable of describing the dynamics associated with the flapping fins. The quasi-steady state computations, with correct incorporation of the experimental kinematics, are useful in determining trends in force production. They do not, however, provide accurate estimates of the magnitudes of the forces produced. Completely unsteady computations about the deforming pectoral fins using experimentally measured fin kinematics gave excellent agreement, both in the time history of force production throughout the flapping strokes and also the magnitudes of the generated forces.

We confirmed the experimental findings on the time of occurrence of the maximum thrust during adduction and maximum lift during abduction. We concluded that 3-D inertial effects are not a minor perturbation, but are critical for accurate force computations. We also observed, through flow visualization throughout the stroke cycle, only a very small flapping-induced inward and outward spanwise velocity, acting over the near-root region of the pectoral fin. We observed a large recirculation region in the junction of the pectoral fin and the body that extends to almost half the span and is present throughout the cycle of oscillation. During the downstroke, maximum thrust and lift forces occur at approximately 32% and minimum thrust is produced at 84% of the downstroke. The thrust reaches a maximum at approximately 68% of the upstroke. The velocity vectors indicate the presence of a large leading edge vortex, the shedding of a pair of counter-rotating vortices at the end of the upstroke from the distal edge, and the shedding of a trailing-edge vortex midway during the upstroke. We did not observe a spiral leading-edge vortex on the pectoral fin. The pectoral fin flapping flow was dominated by the strong axial flow, as opposed to the flows in hovering insects such as the hawkmoth, where an attached leading-edge spiral vortex has been shown to be important in high lift generation. In pectoral fin flapping associated with swimming against a strong current, the primary need for the wrasse is to attain the axial acceleration necessary for high-speed forward motion, and some vertical position changes can be tolerated. It is possible that during hovering or low-speed maneuvering, where vertical position-keeping is more important, wrasse pectoral fin flows are more like those of the hawkmoth or *Drosophila*.

References

Drucker, E. G. and Lauder, G. V. (1999). Locomotor forces on a swimming fish: three-dimensional vortex wake dynamics quantified using digital particle image velocimetry. *J. Exp. Biol.* **202**, 2393-2412.

Drucker, E. G. and Lauder, G. V. (2000). A hydrodynamic analysis of fish swimming speed: wake structure and locomotor force in slow and fast labriform swimmers. *J. Exp. Biol.* **203**, 2379-2393.

Ellington, C. P., Van den Berg, C. and Willmott, A. P. (1996). Leading-edge vortices in insect flight. *Nature* **384**, 626-630.

Löhner, R. (1988). An adaptive finite element solver for transient problems with moving bodies. *Comput. Struct.* **30**, 303-317.

Ramamurti, R. and Löhner, R. (1992). Evaluation of an incompressible flow solver based on simple elements. In *Advances in Finite Element Analysis in Fluid Dynamics*, FED vol. 137 (ed. M. N. Dhaubhadel, M. S. Engleman and J. S. Reddy), pp. 33-42. New York: ASME Publication.

Ramamurti, R. and Sandberg, W. C. (2002). A 3-D computational study of aerodynamic mechanisms of insect flight. *J. Exp. Biol.* **205**, 1507-1518.

Ramamurti, R., Löhner, R. and Sandberg, W. C. (1994). *Evaluation of a Scalable 3-D Incompressible Finite Element Solver. AIAA Paper* No. *94-0756*.

Ramamurti, R., Löhner, R. and Sandberg, W. C. (1995). *Simulation of a Torpedo Launch Using a 3-D Incompressible Finite Element Flow Solver. AIAA Paper* No. *95-0086*.

Ramamurti, R., Löhner, R. and Sandberg, W. C. (1996). Computation of unsteady flow past a tuna with caudal fin oscillation. In *Advances in Fluid Mechanics*, vol. 9 (ed. M. Rahman and C. A. Brebbia), pp. 169-178. Southampton, UK: Computational Mechanics Publications.

Ramamurti, R., Löhner, R. and Sandberg, W. C. (1999). Computation of the 3-D unsteady flow past deforming geometries, *Int. J. Comp. Fluid Dyn.* **13**, 83-99.

Ramamurti, R. and Sandberg, W. C. (2001). Simulation of flow about flapping airfoils using a finite element incompressible flow solver, *AIAA J.* **39**, 253-260.

Sandberg, W. C. and Ramamurti, R. (1999). Unsteady flow computational technology for flapping fins: a status report. In *Proc. Unmanned Undersea Submersibles Technology Symposium*, pp. 182-194. Durham, NH: Autonomous Undersea Systems Institute.

Sandberg, W. C., Ramamurti, R., Westneat, M. W. and Walker, J. A. (2000). 3-D Computations of Flapping Aquatic Flight, *Proc. First Intl Symp. on Aqua-Bio Mechanisms*, p. 184. Honolulu, HI: Tokai University Pacific Center.

Walker, J. A. (1998). Estimating velocities and accelerations of animal locomotion: A simulation experiment comparing numerical differentation algorithms. *J. Exp. Biol.* **201**, 981-995.

Walker, J. A. and Westneat, M. W. (1997). Labriform propulsion in fishes: kinematics of flapping aquatic flight in the bird wrasse, *Gomphosus varius* (Labridae), *J. Exp. Biol.* **200**, 1549-1569.

Walker, J. A. and Westneat, M. W. (2000). Mechanical performance of aquatic rowing and flying. *Proc. R. Soc. Lond. B* **267**, 1875-1881.

Walker, J. A. and Westneat, M. W. (2002a). Performance limits of labriform propulsion: a comparison between rowers and flappers. *J. Exp. Biol.* **205**, 177-187.

Walker, J. A. and Westneat, M. W. (2002b). Erratum: Performance limits of labriform propulsion and correlates with fin shape and motion. *J. Exp. Biol.* **205**, 707.

Westneat, M. W. (1996). Functional morphology of aquatic flight in fishes: mechanical modeling, kinematics, and electromyography of labriform locomotion. *Amer. Zool.* **36**, 582-598.

Willmott, A. P., Ellington, C. P. and Thomas, A. L. R. (1997). Flow visualization and unsteady aerodynamics in the flight of the hawkmoth, *Manduca sexta*. *Phil. Trans. R. Soc. Lond. B* **352**, 303-316.

View publication stats